International Journal of Fatigue 92 (2016) 25–35

Contents lists available at ScienceDirect

International Journal of Fatigue

journal homepage: www.elsevier.com/locate/ijfatigue

Multiaxial high-cycle fatigue criteria and life prediction: Application to gas turbine blade

W. Maktouf [a,c], K. Ammar [b], I. Ben Naceur [c], K. Saï [c,*]

[a] Lead Mechanical Engineer, Mechanical ATA, BG Tunisia, Tunisia
[b] MINES ParisTech, Centre des Matériaux, CNRS UMR 7633, BP 87, 91003 Evry Cedex, France
[c] UGPMM, Ecole Nationale d'Ingénieurs de Sfax, BP 1173 Sfax, Tunisia

ARTICLE INFO

Article history:
Received 1 April 2016
Received in revised form 18 June 2016
Accepted 24 June 2016
Available online 27 June 2016

Keywords:
Turbine blade
Inconel 718
FEA
High-cycle fatigue
Multiaxial loading
Life estimation

ABSTRACT

A recent work conducted by the authors (Maktouf and Saï, 2015) demonstrated that the root cause of the premature blade failure was caused by high-cycle fatigue (HCF) mechanism initiated at a localized carbon-rich area inducing grain boundary brittleness. The blade was subject to multiaxial cyclic loadings during its service life and any attempt to assess component fatigue strength leads to the question of choosing an appropriate fatigue design criterion. In this paper several multiaxial fatigue models are applied as post-processing step of the Finite Element Analysis (FEA) output results and the estimated fatigue lifetimes were assessed under different loading conditions. The material fatigue parameters, required as an input to the selected fatigue models were determined through a series of bending and torsion tests on specimens made of aged Inconel 718. A numerical post-processing algorithm was developed for Fatemi-Socie fatigue criterion and included as additional post-computation model in the used computer aided fatigue damage evaluation tool. The authors point out that the majority of the multiaxial fatigue studies available in the literature are conducted mainly for correlating the experimental laboratory results on specimens while they have been used in the frame of this study to investigate their application to an industrial case.

1. Introduction

In a recent work, the authors investigated through mechanical, metallography and chemical analysis an industrial case of premature fatigue failure of gas turbine blade [1]. The root cause was attributed to fatigue cracks initiated near the airfoil leading edge and propagated towards airfoil mid-chord until final tensile overload separation occurred. This blade experienced multiaxial cyclic loadings during its service life and damage was attributed to high-cycle fatigue (HCF) mechanism causing grain boundary brittleness. The latter was found initiated at a localized carbon-rich area considered as metallurgical anomaly region that originated during component fabrication phase.

Furthermore, the recorded high incidence of HCF related failures of gas turbine blades [2,3] under multiaxial loading conditions imposes a requirement for an accurate evaluation of blades' material capability under HCF. The component's geometry under multiaxial stress states should then be evaluated with an adequate multiaxial fatigue model for an accurate component fatigue lifetime estimation. Although several research studies have been conducted in this subject, uncertainties still exist as to which multiaxial fatigue model should be used for a particular material and geometry and under a given loading condition. It should be pointed out that the majority of the multiaxial fatigue studies were conducted for correlating the experimental laboratory results on specimens and that a few studies investigated the application of the developed approaches to an actual design for industrial components. To note also that for this schematic, there is no attempt to assess the damage present in the form of initial material or manufacturing defects nor the evaluation of the propagation life as a fraction of component total life. Main focus is for assessing the HCF failure developed during service operation which requires a relatively large fraction of life to initiation.

As stated above, an initial review of the developed multiaxial fatigue models was conducted. Several comparative and evaluation studies are available in the literature [4–14]. Obviously, the aim of the multiaxial fatigue models is to reduce the complex multiaxial loading into an equivalent uniaxial loading where material data from simple and/or uniaxial laboratory tests could be used in computer aided algorithms combined with the finite element method (FEM) for crack initiation life predictions. To authors' knowledge

* Corresponding author.
E-mail address: kacemsai@yahoo.fr (K. Saï).

http://dx.doi.org/10.1016/j.ijfatigue.2016.06.024
0142-1123/

there are no universal categorization of the developed multiaxial fatigue models: Multiaxial fatigue theories have been classified initially into five viewpoints [5]: (i) empirical formulas and modifications of the Coffin-Manson equation, (ii) application of stress or strain invariants, (iii) use of the space averages of stress or strain, (iv) critical plane approaches and (v) use of accumulated material's energy. Chen et al. [13] classified the multiaxial fatigue damage models into three main categories: stress-strain based approach, the energy based approach and the critical plane approach. Liu and Mahadavan [14] assumed that the stress-based approaches could be further divided into four sub-categories: empirical equivalent stress, stress invariants, average stress and critical plane stress.

Based on the reviewed literature and the several developed multiaxial fatigue criteria, authors classify the models into four categories based on the physical quantities used in the theories:

- Stress-based models which are applicable for HCF regime where plastic strains are insignificant.
- Strain-based models applicable for both LCF and HCF regimes. These approaches are purely based on strain quantities and couldn't then consider the non-proportional loadings effect causing material hardening and requiring additional stress response in the formulas.
- The energy concept based on the energy quantities assessing the material fatigue failure. It uses a combination of the plastic strain energy with the plastic deformation in a continuous fatigue accumulation formulas.
- The "shear strain"-stress based criterion which includes a combination of strain and stress values.

Critical plane concepts are then covered by the above categories and are defined by the used critical physical quantities. As an example, Findley et al. [15] defined the plane subject to the largest cycle of shear stress as the critical plane, while Fatemi and Socie [16] defined the critical plane as the plane associated with the maximum shear strain amplitude. For an adequate selection of the applicable multiaxial fatigue model, the component subject to multiaxial stress states should be verified if it is subject to proportional (In-phase) or non-proportional (Out-phase) loading. Proportional loading is characterized by fixed principal axes direction during the loading cycle. While for non-proportional loading, the orientation of the principal normal stress axes continuously change with respect to the loading axes and often produces additional cyclic hardening and shorter fatigue life in opposite to the proportional loading. For our industrial case, the blade is assumed subject to proportional loading (centrifugal and aerodynamic loads) where stress components vary proportionally with time and the principal stress directions remain fixed.

In the frame of this study, four multiaxial fatigue models are then selected, assessed and compared for lifetime estimation of the gas turbine blade: Sines, Crossland, Dang Van and Fatemi-Socie criteria. Computer aided fatigue damage evaluation of the component consisted of two phases: Dynamic stress computation obtained from the Finite Element Model (FEM) simulations and the fatigue life prediction carried out as post-processing step of the Finite Element Analysis (FEA) output results.

This paper starts by determining the material fatigue parameters, required as an input to the selected fatigue models, through a series of bending and torsion tests on specimens. Approximation methods were also used to estimate the remaining parameters required for the Fatemi-Socie model (Section 2). Section 3 details the selected fatigue models and the related material parameters to include in the computer aided fatigue algorithms. Section 4 is devoted to the FEA of the component and the results of post-processing calculations. The last section aims at providing a comparison of the fatigue model calculations and a conservative lifetime estimation of the component.

2. Experiments

2.1. Material, specimens and test procedure

The failed blades were made of UNS N07718 material (Formerly Grade 718) which is a Ni-Cr-Fe-Nb alloy. The chemical composition complying with ASTM B637 requirements is prescribed in Table 1. ASTM B637 Alloy 718 product is available in forged bar, blank, ring, and rolled bar. The material is heat treated by solution and precipitation hardening. The recommended heat treatment as specified in the ASTM standard is solution treatment at a temperature of 924–1010 °C (1700–1850 °F), hold for at least half hour and then cooled down at rate equivalent to air cool or faster. This heat treatment is to be followed by precipitation hardening treatment at a temperature of 718 ± 14 °C (1325 ± 25 °F), hold at temperature for 8 h, cool down to 621 ± 14 °C (1150 ± 25 °F), and hold until total precipitation heat treatment time has reached 18 h then air cooled down to room temperature. Inconel 718 alloy differentiates from other Nickel based super-alloys with the relatively high contents of iron [Fe-19%] and Niobium (or Columbium) [Nb-5%].

The folowing experiments have been conducted on specimens machined from rolled bar of 107 mm diameter. Raw material is solution annealed and age hardened as described above (ASTM B637 requirements):

- Magnification micrograph examination of the raw material microstructure.
- Brinell Hardness Measurements.
- Uniaxial tensile test.
- Fatigue tests on smooth cylindrical specimens: Pure alternated bending ($R = -1$); repeated bending ($R = 0$) and alternated torsion ($R = -1$).

The magnification micrograph examination of the material microstructure was carried out on specimens extracted from three locations in the radial-cross section of the bar: (i) center of the bar, (ii) mid radius region and (iii) outer part. Specimens are prepared in compliance to the NFA-05-150 standard: Final polishing with 1 μm DIAMAT diamond on GOLDPAD polishing pad and etching with Kalling's reagent.

Table 1
Chemical composition of UNS N07718 – ASTM B637.

Element	Composition Limits, %	Product(Check) Analysis Variations, Under min or Over max, of the Specified Limit of Element
	UNS N07718 (Formerly Grade 718)	
Carbon	0.08 max	0.01
Manganese	0.35 max	0.03
Silicon	0.35 max	0.03
Phosphorus	0.015 max	0.005
Chromium	17.0–21.0	0.25
Cobalt	1.0 max	0.03
Molibdenum	2.8–3.3	0.05 under min, 0.10 over max
Columbium (Nb) + tantalum	4.75–5.50	0.15 under min, 0.20 over max
Titanium	0.65–1.15	0.04 under min, 0.05 over max
Aluminium	0.20–0.80	0.05 under min, 0.10 over max
Boron	0.006 max	0.002
Iron	Remainder	...
Copper	0.30 max	0.03
Nickel	50.0–55.0	0.35

Hardness measurements were taken in the outer part of the bar in compliance with the standard NF EN ISO 6506-1(Brinell)/ASTM E-10. The used bench hardness tester is AFFRI 270 Integral with indentation VEB HP 0250 308/389. The test Load is 1839 N.

Uniaxial tensile tests have been conducted on two cylindrical specimens (see Fig. 1). The material mechanical properties such Young modulus, ultimate tensile strength, yield limit and elongation at failure have been identified.

In order to understand the material cyclic behavior and assess the component fatigue lifetime under complex loading conditions including variable amplitudes (damage accumulation) and multiaxial loads, tests should be conducted to determine the material fatigue characteristics which are essential inputs to several available fatigue models. Therefore, fatigue tests are carried-out on un-notched cylindrical specimens (see Figs. 2 and 3) for three loading conditions: pure alternated bending ($R = -1$), repeated bending ($R = 0$) and alternated torsion ($R = -1$). Material fatigue strength and endurance limits are gathered at lives between 1.10^5 and 2.10^6 cycles.

A maximum value, R_a = 0.8 μm, of specimen's surface roughness has been ensured to reduce the effect of machined surface on the test results. The same geometry and surface roughness has been used for both bending and torsion tests. Sinusoidal type loading has been conducted, at room temperature, on (15) specimens for each type of fatigue test. Specimen failure is considered when a crack of about 0.5 mm depth is detected on the 12 mm specimen diameter. A servo-hydraulic multi-actuators fatigue testing machine (Fig. 4) has been used for both bending and torsion fatigue tests at a testing frequency of 50 Hz.

Machine testing capabilities are 210 N m for plane bending, 150 N m for rotating bending and 150 N m for torsion. Testing frequency is up to 60 Hz. Bending is imposed by two servo-hydraulic actuators generating moments in perpendicular planes to the specimen. Torsion is imposed by a third hydraulic actuator (Fig. 5a). The generation of the bending moment applied to the specimen is based on the principle of rotating fields [17]. The specimen does not rotate while two servo-hydraulic actuators A and B imposes two plane bending moments (four support points without shear force) in two perpendicular planes (Fig. 5b). The resulting bending load could be:

- Plane bending: When two actuators are acting in phase or only one jack is active.

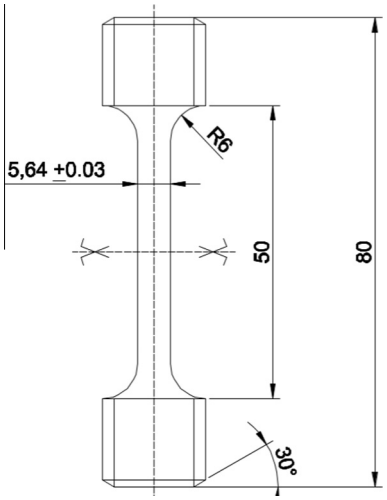

Fig. 1. Tensile test specimen geometry #1.

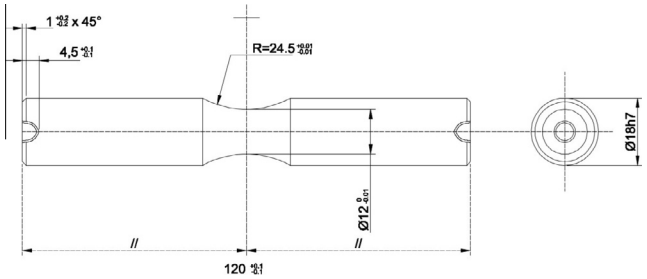

Fig. 2. Fatigue test specimen geometry #2.

Fig. 3. Fatigue specimen's picture.

- Rotating bending: When two actuators are acting with a phase angle of 90°.

A third hydraulic actuator T imposes a torsion moment on a beam which consists of the specimen to be tested (Item#1 – Fig. 5a) and two half beams (Item#2 and Item#2′ – Fig. 5a). This beam contains the two plane bending moment sensors on the half beam (Item#2′) and one torsion moment sensor on the other half beam (Item#2). Moment sensors are initially static calibrated and then dynamic calibrated using the specimen to be tested (Material and Geometry).

2.2. Experimental results and discussions

In this section experimental results of the above specified static and dynamic experiments are presented and an initial interpretation is briefly highlighted.

2.2.1. Magnification micrograph examination of the raw material microstructure

High magnification and detailed views of the metallographic structure of the specimens extracted from three locations in the radial-cross section of the bar are represented in Figs. 6–8.

Samples taken from the center of the bar show a grain size of ASTM #6 in accordance to ASTM E112 (Fig. 6). Gamma double prime γ'' (Ni3Nb) phase which is the predominate strengthening phase appears as disc shaped and has ordered body-centered tetragonal (BCT) crystal structure. Carbides of type MC is useful in aiding structural refinement during the fabrication and heat treatment by assisting in grain size control. They strengthen the matrix when present in grain boundaries area. Conversely, a large amount of precipitates with irregular shapes and forming continuous network along the grain boundaries are a source of dislocations and initiation of fatigue cracks. Sample taken from the mid radius region of the bar show smaller grain size of ASTM #7.5 (Fig. 7). Sample taken from the outer region of the bar show the smallest grain size of ASTM #9 (Fig. 8). The raw nickel-based alloy 718 was provided of premium quality. Micrograph examination of samples taken from different locations of the bar section confirms that grain sizes vary from ASTM #6 to ASTM #9 and that precipitations such carbides (MC) are of regular morphology and with very

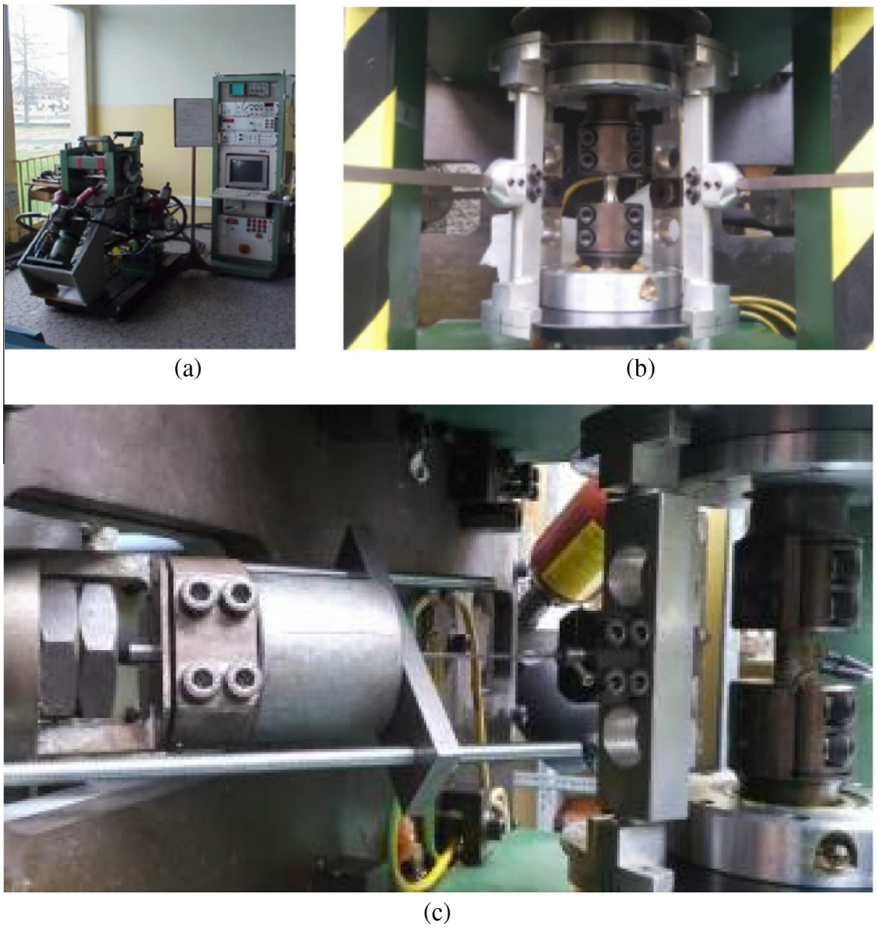

Fig. 4. Testing machine: (a) Fatigue testing machine. (b) Specimen fixture device. (c) Bending hydraulic actuator-A.

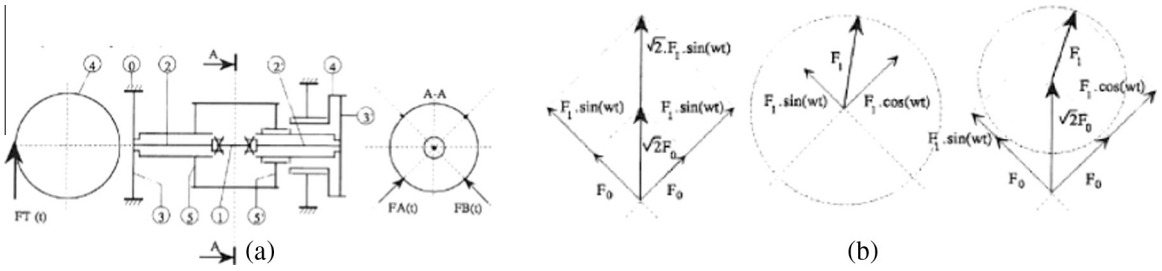

Fig. 5. Mechanism of the fatigue testing machine: (a) Mechanical scheme of the fatigue testing machine. (b) Principle of the two perpendicular plane bending moments [17].

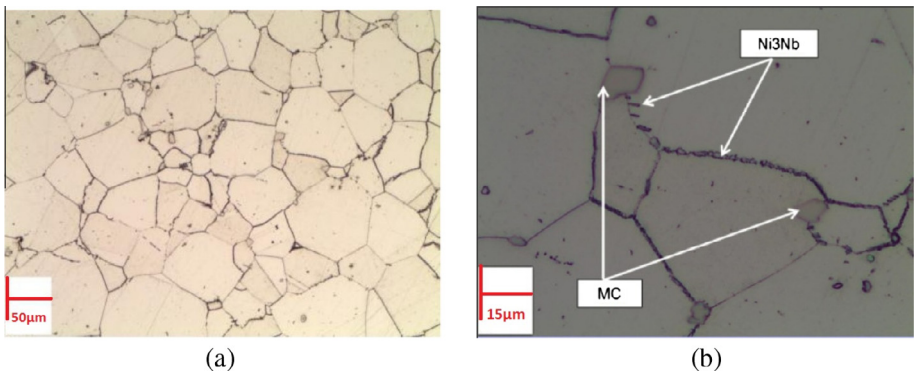

Fig. 6. Microstructure of specimen from the center of the bar: (a) High magnification view. (b) Detailed view.

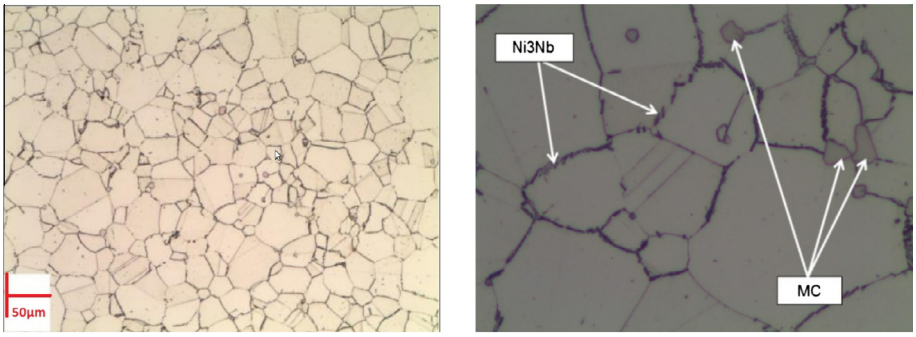

Fig. 7. Microstructure of specimen from the mid-center of the bar: (a) High magnification view. (b) Detailed view.

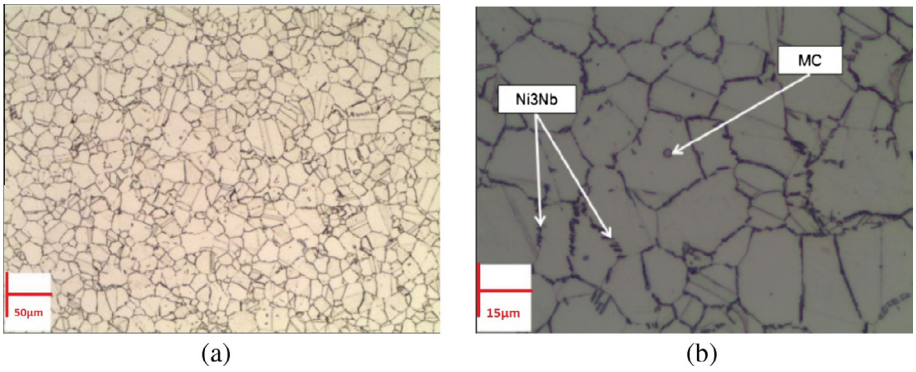

Fig. 8. Microstructure of specimen from the outer region of the bar section: (a) High magnification view. (b) Detailed view.

low ratio/quantities within the grains or along the grain boundaries. However the microstructe of the failed blade [1] presents large amount of precipitates along the grain boundaries. Both microstructure are typical of a heat-treated alloy to ASTM B637 and the blade's microstructure was of grain sizes varying from ASTM #5 to ASTM #9. Fig. 9 compares the free from defect microstructure (Investigated raw material) to the microstructure of the anomaly area in the leading edge of the failed blade. It shows clearly the difference in distribution of precipitations along the grain boundaries and confirms the conclusion of the technical paper [1].

2.2.2. Brinell hardness measurements

The measured mean hardness value (Brinell) was found 415.3 HB. Table 2 summarizes the experimental measurements and the calculated mean value.

Table 2
Hardness test results.

Location	Hardness values (HB 2.5/187.5)	Mean hardness
Outer part	413.0–413.0–419.9–415.3–415.3	415.3

2.2.3. Uniaxial tensile test

Results of the uniaxial tensile tests conducted on two specimens as decribed in subSection 2.1 are shown in Figs. 10 and 11. Material monotonic properties have been identified and summarized in Table 3.

The available experimental tensile properties and material hardness could be used to estimate and approximate the cyclic material fatigue properties (e.g. fatigue strength exponent, fatigue ductility coefficient, etc.) in the absence of the related fatigue tests

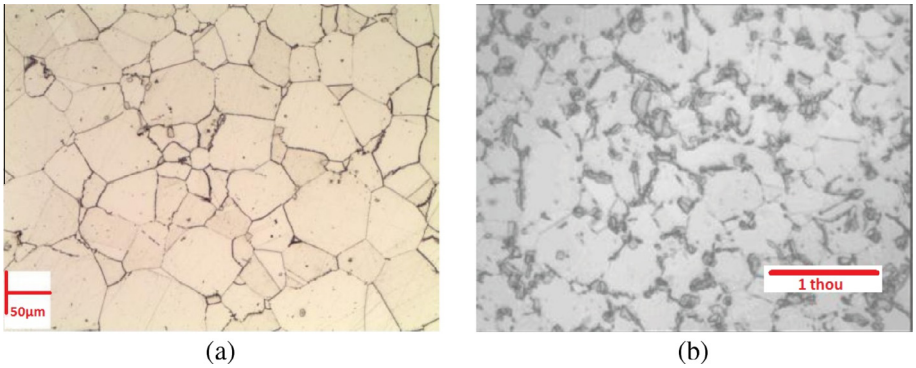

Fig. 9. Comparison of the defect-free microstructure with failed blade's microstructure: (a) High magnification view of raw material. (b) Microstructure of the blade's anomaly region.

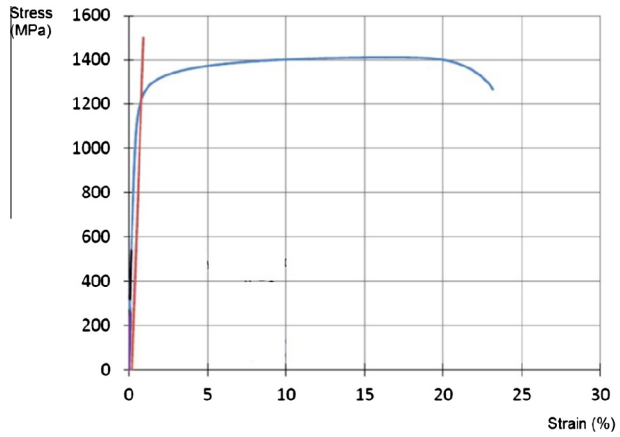

Fig. 10. Stress-strain tensile curve – Specimen 1.

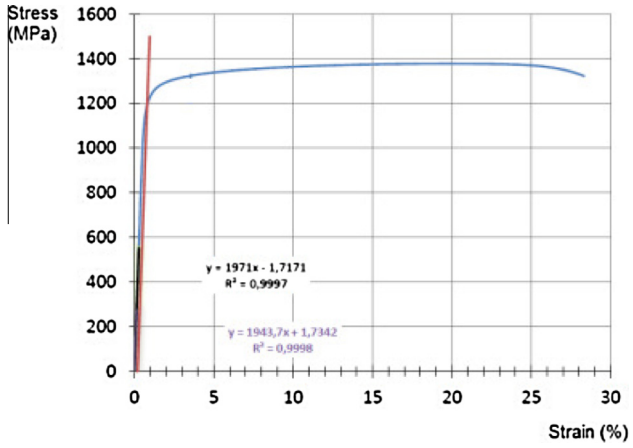

Fig. 11. Stress-strain tensile curve – Specimen 2.

[18]. Several multiaxial fatigue models requiring such inputs and representing the identified damage mechanism could then be used with the approximated cyclic fatigue properties to predict component fatigue live under multiaxial loading. Roessle and Fatemi [19] proposed the following equations to estimate the uniaxial strain-life fatigue properties:

$$\sigma'_f = 4.25(HB) + 225 \quad \varepsilon'_f = \frac{1}{E}\left[0.32(HB)^2 - 487(HB) + 191,000\right]$$
$$b = -0.09 \quad c = -0.56 \tag{1}$$

where σ'_f, ε'_f, b and c are the estimated fatigue strength coefficient, the fatigue ductility coefficient, the fatigue strength exponent and the fatigue ductility exponent, respectively. HB is the measured material Brinell hardness.

Although Roessle and Fatemi did not derive their approximation for nickel based alloys, additional studies compared the observed fatigue lives versus the predicted fatigue lives made using fatigue properties estimated by the Roessle and Fatemi hardness method and results for nickel based alloy were found satisfactory [18,20].

Muralidharan and Manson [21] estimated strain-life fatigue properties based on material tensile properties as following:

$$\sigma'_f = 0.623E\left(\frac{\sigma_u}{E}\right)^{0.832} \quad \varepsilon'_f = 0.0196\varepsilon_f^{0.155}\left(\frac{\sigma_u}{E}\right)^{-0.53}$$
$$b = -0.09 \quad c = -0.56 \tag{2}$$

ε_f is the true fracture ductility and σ_u is the ultimate strength. Baumel and Seeger [22] estimated fatigue properties based on a uniform material law:

$$\sigma'_f = 1.5\sigma_u \quad \varepsilon'_f = 0.59\Psi, \quad b = -0.087$$
$$c = -0.58, \quad \Psi = 1 \quad for \quad \frac{\sigma_u}{E} \le 0.003,$$
$$\Psi = 1.375 - 125\left(\frac{\sigma_u}{E}\right) \quad for \quad \frac{\sigma_u}{E} > 0.003 \tag{3}$$

Considering the results of the experimental static tests conducted on Inconel 718, and using the above described approximation models Eqs. (1)–(3), the uniaxial cyclic fatigue properties of Inconel 718 are estimated and summarized in the Table 4. These properties could be combined, in the absence of experimental fatigue data, with the multiaxial fatigue models to predict fatigue lives for shear and tensile failure mode materials under multiaxial loadings. It has been proven that acceptable fatigue life predictions were obtained with the Fatemi-Socie strain-stress based critical plane approach and fatigue properties estimated from the so called "Baumel-Seeger, Muralidharan-Manson, or Roessle-Fatemi" method [18].

2.2.4. Fatigue test results

The stress-life curves determined from the conducted fatigue tests described in Section 2.1 are presented in Figs. 12–14 and refer to the three loading conditions: pure alternated bending ($R = -1$), repeated bending ($R = 0$) and alternated torsion ($R = -1$). Since fatigue test results are widely scattered especially for HCF region, several probabilistic models were available in the literature to estimate the *S-N* curve considering its scatter [23,24]. In this section, and for each loading configuration, stress life curves were simulated using the Stromeyer, Palmgren and Bastenaire models [25]. For both reversed and repeated bending, the Stromeyer model Eq. (4) was retained for the *S-N* trend.

$$N = \frac{A}{S - E} \tag{4}$$

where S and N are respectively the endurance stress (MPa) and life to failure (Cycles). Constant "A" equals to $42.5\ 10^6$ for reversed bending and $29.1\ 10^6$ for repeated bending test. Constant "E" equals to 511.86 MPa for reversed bending and 357.64 MPa for repeated bending test.

To note that during the repeated bending experimental tests, two specimens did not fail at a high stress level of 440 MPa. These

Table 3
Material monotonic properties.

Parameter	Value
Young modulus, E (MPa)	201506
Ultimate Tensile Strength, UTS (MPa)	1359
Yield limit, Rp0.2 (MPa)	1206
Elongation at failure, A (%)	26

Table 4
Estimated fatigue properties of Inconel 718.

Fatigue properties	Roessle-Fatemi model	Muralidharan-Manson model	Baumel-Seeger model
Fatigue strength coefficient, σ'_f	1990.02	1960.86	2038.5
Fatigue ductility coefficient, ε'_f	0.218	0.3962	0.313
Fatigue strength exponent, b	−0.09	−0.09	−0.087
Fatigue ductility exponent, c	−0.56	−0.56	−0.58

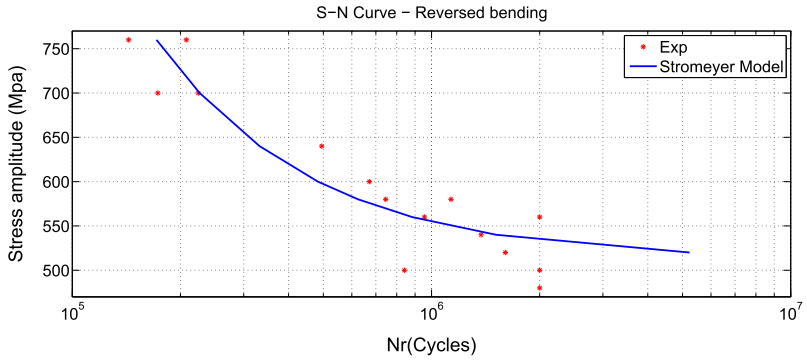

Fig. 12. Reversed bending *S-N* curve according to Stromeyer model.

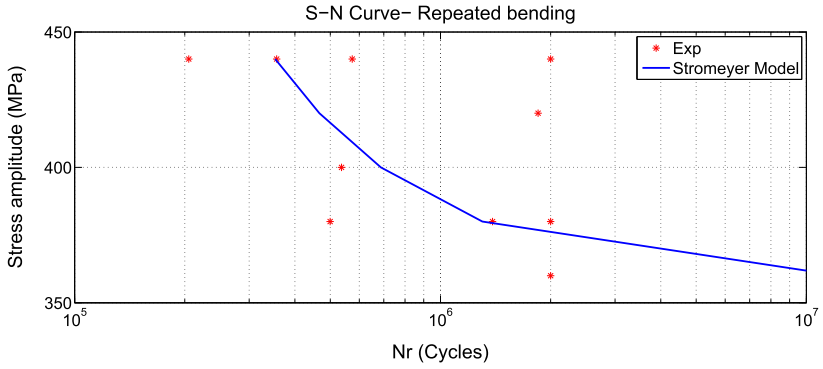

Fig. 13. Repeated bending *S-N* curve according to Stromeyer model.

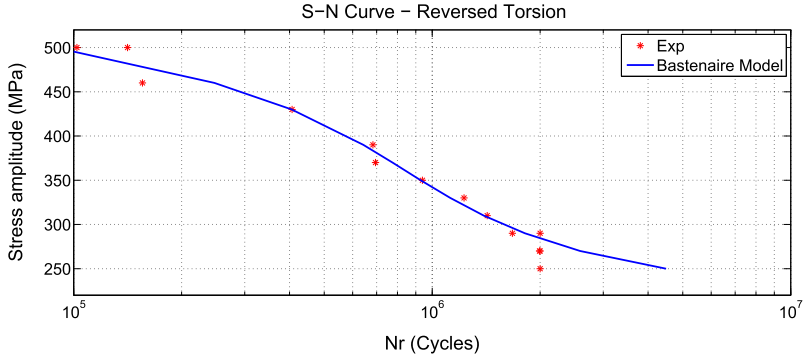

Fig. 14. Reversed torsion *S-N* curve according to Bastenaire model.

results are not coherent and have been excluded from the analysis. Stromeyer model was found fitting better the data comparing to the palmgrean model. The curve of Fig. 13 is the median curve of the 10% and 90% probability of failure curves.

For reversed torsion tests, Bastenaire Eq. (5) suits better the experimental results:

$$N = \frac{A \exp\left(-\left(\frac{S-E}{B}\right)^C\right)}{(S-E)} \tag{5}$$

where $A = 12.22\ 10^8$, $B = 252.29$ MPa, $C = 5$, $E = 222.84$ MPa.

3. Fatigue models for the fatigue assessment of multiaxial stress cycles

The gas turbine blade is made of ductile material (Inconel 718) and is subject to proportional loadings: centrifugal and aerodynamic loads. As stated in Section 1, four multiaxial fatigue criteria have been selected for their suitability and good correlation with the material behavior, dominated loading and failure modes: Sines, Crossland, Dang Van and Fatemi-Socie criteria.

3.1. Sines criterion

Sines criterion [26] is a stress-based criterion calculating the equivalent nominal stress amplitude from the octahedral shear stress and the hydrostatic stress value. The multiaxial stress state is then reduced to an equivalent uniaxial stress state and the calculated equivalent stress value is compared to the uniaxial fully reversed fatigue strength value. This criterion is then relating the second invariant of the stress deviator and the first invariant of the stress tensor. Furthermore, Sines stated that a superimposed mean static torsion has no effect on the fatigue limit of metals subject to cyclic torsion. Sines Criteria is defined by the following formula:

$$\sqrt{\Delta J_{2,alt}} + \beta_s \frac{I_{1,mean}}{3} \leqslant \lambda; \tag{6}$$

where $\Delta J_{2,alt}$ measures the amplitude of the deviatoric stress tensor $\underset{\sim}{\mathbf{S}} = \underset{\sim}{\sigma} - trace(\underset{\sim}{\sigma})/3\,\underset{\sim}{\mathbf{I}}$ and $\mathbf{I}_{1,mean}$ is the mean value of the first invariant of the stress tensor corresponding to the hydrostatic stress during the stress loading cycles. β_s and λ are material parameters defined as following:

$$\lambda = \tau_{alt}$$

$$\beta_s = 3\frac{\tau_{alt}}{f_{rep}} - \sqrt{3}$$

τ_{alt} is the material fatigue strength under reversed torsion and f_{rep} is the fatigue strength value under repeated bending. This criterion is already implemented as post-computation model in the ZeBuLoN Code [27]. Material parameters are calculated from the conducted experiments of Section 2.

3.2. Crossland criterion

Crossland criterion is similar to Sines criterion but includes the maximum hydrostatic pressure instead of the mean value and it is defined by the following formula [28]:

$$\sqrt{\Delta J_{2,alt}} + \beta_c \frac{I_{1,max}}{3} \leqslant \lambda; \tag{7}$$

where $\Delta J_{2,alt}$ measures the amplitude of the deviatoric stress tensor $\underset{\sim}{\mathbf{S}} = \underset{\sim}{\sigma} - trace(\underset{\sim}{\sigma})/3\,\underset{\sim}{\mathbf{I}}$ and $\mathbf{I}_{1,max}$ is the maximum value of the first invariant of the stress tensor corresponding to the hydrostatic stress during the stress loading cycles. β_c and λ are material parameters defined as following:

$$\lambda = \tau_{alt}$$

$$\beta_c = \frac{\tau_{alt}}{f_{alt}} - \sqrt{3}$$

τ_{alt} is the material fatigue strength under reversed torsion and f_{alt} is the fatigue strength value under reversed bending. This criterion is already implemented as post-computation model in the ZeBuLoN Code [27]. Material parameters are calculated from the conducted experiments of Section 2.

3.3. Dang Van criterion

The Dang Van's criterion [29] is considered as a critical plane approach since it searches the maximum shear stress amplitude at all instants (t_i) and in all physical space directions ($\vec{n}$). Both the classical Dang Van criterion (DV1) and the modified Dang Van criterion (DV2) are used in post-processing calculations.

- The classical Dang Van criterion (DV1) is defined as following:

$$\max_{\vec{n}}\left[\max_{t}[\tau + \alpha p]\right] \leqslant \tau_{alt}; \tag{8}$$

  where $\alpha = 3\left(\frac{\tau_{alt}}{\sigma_{alt}} - \frac{1}{2}\right)$; τ_{alt} is the fatigue limit in pure alternating torsion, σ_{alt} is the fatigue limit in alternate bending. τ is the current shear stress component in a plane defined by its normal $\vec{n}$ and p is the current hydrostatic pressure.
- The modified Dang Van criterion (DV2): It simplifies the post-processing calculation by determining the maximum value of the von Mises invariant over the time instead of scanning the shear stress values at all planes defined by its normal $\vec{n}$:

$$\max_{t}[DJ_2(t_i) + \alpha p] \leqslant \tau_{alt}; \tag{9}$$

  where $DJ_2(t_i)$ is the von Mises invariant of the difference in current stress and σ_0. σ_0 corresponds to loading path center. $\alpha = 3\left(\frac{\tau_{alt}}{\sigma_{alt}} - \frac{1}{2}\right)$; τ_{alt} is the fatigue limit in pure alternating torsion, σ_{alt} is the fatigue limit in alternate bending.

The criteria DV1 and DV2 are already implemented as post-computation models in the ZeBuLoN Code [27]. Material parameters are calculated from the conducted experiments of Section 2.

3.4. Fatemi-Socie criterion

Fatemi and Socie criterion [16,30] is a "shear strain"-stress based criterion where the critical plane is defined by the plane associated with the maximum shear strain amplitude. The fatigue damage value is calculated as per Eq. (10):

$$\gamma_{max}\left(1 + K\frac{\sigma^n_{max}}{\sigma_y}\right) = D_{FS} \tag{10}$$

where

- γ_{max}: Maximum shear strain (Primary parameter driving the crack).
- K: Material constant (Designated as normal stress sensitivity).
- D_{FS}: Criterion's fatigue damage value (designated as "uniaxial effective shear strain amplitude").
- σ_y: Yield strength.
- $\sigma^n_{max} = \sigma^n_a + \sigma^n_m$: The maximum value of the normal stress to the maximum shear strain plane (Secondary parameter).
- σ^n_a: Alternating normal stress value.
- σ^n_m: Mean normal stress value.

The uniaxial effective shear strain amplitude D_{FS} is related to the number of cycles to failure and obtained through the Basquin-Manson-Coffin Eqs. (11) and (12):

$$\varepsilon_{a,eq} = \frac{\sigma'_f}{E}(2N_f)^b + \varepsilon'_f(2N_f)^c \tag{11}$$

$$D_{FS} = \frac{\tau'_f}{G}(2N_f)^{b'} + \gamma'_f(2N_f)^{c'} \tag{12}$$

where

- σ'_f: Fatigue strength coefficient.
- b: Fatigue strength exponent.
- ε'_f: Fatigue ductility coefficient.
- c: Fatigue ductility exponent.
- $\tau'_f \approx \sigma'_f/3^{1/2}$; $b' \approx b$; $\gamma'_f \approx \varepsilon'_f/3^{1/2}$; $c' \approx c$.

The Fatemi-Socie criterion is not implemented as part of the available post-computation models of the ZeBuLoN Code. It was then developed using Zlanguage which is a ZeBuLoN scripting language (C++ basis). The used steps for elaborating the criterion's algorithm are described below:

Step 1: Determine the stress $\underset{\sim}{\sigma}(t)$ and strain $\underset{\sim}{\varepsilon}(t)$ tensors at each material point (Gauss point) of the blade geometry during the loading cycle (Finite Element Analysis). To find the maximum shear strain amplitude, max γ_a, we should take into account all the planes passing through the material point which is located by its normal vector $\vec{n}$, and described by its spherical angles (ϕ, θ). To reduce to the minimum the time necessary for completing the

calculation by avoiding the scan of all the planes, a post-processor tool (process-range) is used to calculate the amplitude of a scalar or tensorial variable from its history. For our case of a tensorial variables $\underset{\sim}{\sigma}$ and $\underset{\sim}{\varepsilon}$, an invariant of the type von Mises is used to calculate the space distance in the six different dimensions, and the result is the diameter of the smallest sphere encompassing the point of interest's path during the loading. This provides the mean value of the stress and strain during a load cycle.

Step 2: Calculation of the eigenvalues and eigenvectors of the strain tensor. Eigenvalues are arranged in ascending order. The eigenvector $\overrightarrow{V_I}$ corresponds to the largest eigenvalue. The eigenvector $\overrightarrow{V_{III}}$ corresponds to the smallest eigenvalue and the eigenvector $\overrightarrow{V_{II}}$ corresponds to the remaining eigenvalue.

Step 3: Projecting stress $\underset{\sim}{\sigma}(t)$ and strain $\underset{\sim}{\varepsilon}(t)$ tensors to the eigenvectors' directions:

- $\varepsilon_I = \overrightarrow{V_I} * (\underset{\sim}{\varepsilon} * \overrightarrow{V_I})$;
- $\varepsilon_{II} = \overrightarrow{V_{II}} * (\underset{\sim}{\varepsilon} * \overrightarrow{V_{II}})$;
- $\varepsilon_{III} = \overrightarrow{V_{III}} * (\underset{\sim}{\varepsilon} * \overrightarrow{V_{III}})$;
- $\sigma_I = \overrightarrow{V_I} * (\underset{\sim}{\sigma} * \overrightarrow{V_I})$;
- $\sigma_{II} = \overrightarrow{V_{II}} * (\underset{\sim}{\sigma} * \overrightarrow{V_{II}})$;
- $\sigma_{III} = \overrightarrow{V_{III}} * (\underset{\sim}{\sigma} * \overrightarrow{V_{III}})$;
- $\underset{\sim}{\varepsilon}(t) = [\varepsilon_I, \varepsilon_{II}, \varepsilon_{III}, 0, 0, 0]$ in $(\overrightarrow{V_I}, \overrightarrow{V_{II}}, \overrightarrow{V_{III}})$ coordinates and $\varepsilon_I, \varepsilon_{II}$ and ε_{III} are the eigenvectors;
- $\underset{\sim}{\sigma}(t) = [\sigma_I, \sigma_{II}, \sigma_{III}, \sigma_{12}, \sigma_{13}, \sigma_{23}]$ in $(\overrightarrow{V_I}, \overrightarrow{V_{II}}, \overrightarrow{V_{III}})$ coordinates.

Step 4: Calculate the maximum shear strain γ_{max} in the critical plane: $\gamma_{critical} = (\varepsilon_I - \varepsilon_{III})/2$.

Step 5: Calculate the maximum stress in the plane perpendicular to the critical plane: $\sigma_n = (\sigma_I + \sigma_{III})/2$.

Step 6: Determine the fatigue damage value D_{FS} and the number of cycles to failure N_f.

The intent of the developed algorithm is to determine the fatigue damage value as defined by Fatemi-Socie criterion but not to identify the critical plane defined by the pair (ϕ^*, θ^*) values that provides the maximization of the problem above. The Criteria material parameters are determined from Section 2.

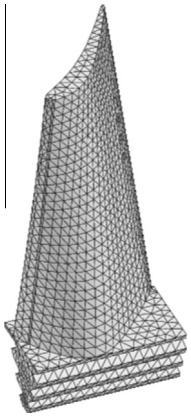

Fig. 15. GT blade meshing.

4. FEM and post-processing calculations

The finite element (FE) analysis of the gas turbine blade's geometry has been performed using the Mesher and FE modules of ZeBuLoN. C3D4 quadratic tetrahedron elements were used for the mesh generation (Fig. 15). The mesh consists of (12521) elements and (3210) nodes. The identified experimental mechanical properties of Inconel 718 has been included in the model. The applied boundary conditions were centrifugal and aerodynamic loads as detailed in Sections 5.1 and 5.2 of the technical paper [1]. The stress due to centrifugal load is the main critical load acting on the blade and depends on two variable parameters: the whirling rotor speed and the distance of each element from the rotating axis. Aerodynamic loads includes the blade passage flow characterized by the boundary layer effects and flows generated by the passage pressure gradients. The complex stresses generated by vortical flow such as: the leading edge "horse-shoe" vortices, tip-leakage flow vortices and corner vortices were neglected comparing to the centrifugal and blade's mid span pressure gradients. Aerodynamic stresses depend on the blade/vane passage and are alternating between two-off stator vanes.

A loading cycle includes engine start-up and acceleration to a cranking speed of 1200 tr/min during 20 s, then maintained at this speed for 820 s. The firing and acceleration phase to the self sustained speed of 8000 tr/min yields to a proportional increase in centrifugal and aerodynamic loads on the compressor blades. The loading cycle ends with rotor deceleration and engine shutdown.

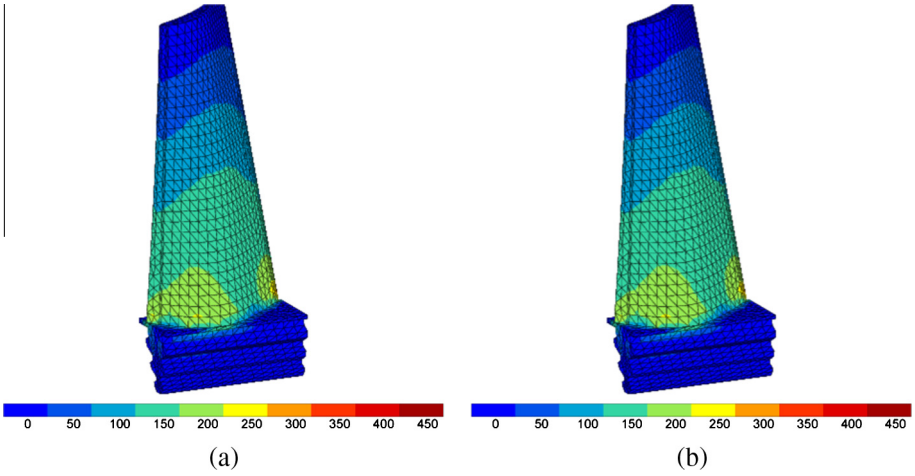

Fig. 16. Maximum and minimum von Mises stress of the rotating blade (a) Blade in midway between stators' vanes (365 MPa). (b) Blade aligned with stator vane (362.8 MPa).

The FEA of the blades shows that during steady state conditions (self sustained speed), the maximum von Mises stress was alternating between 365 MPa when the rotor blade is in the midway between two stator vanes and 363 MPa when it is aligned with the stator vane (Fig. 16). Post-calculation of the FEA results has been conducted to calculate the Sines, Crossland and Dang Van equivalent stress value and the Fatemi-Socie fatigue damage value. For Sines, Crossland and Dang Van criteria, the calculated values are used with the corresponding uniaxial fatigue limits as defined in Eqs. (6) and (7) to estimate the component lifetime. For Fatemi-Socie criterion, the Basquin-Manson-Coffin Eqs. (11) and (12) are used to estimate the component lifetime. Results are summarized in Table 5. As specified in Table 5, the estimated component lifetime vary according to the different criteria due to the fact that the stress-strain fields are processed in different ways respect to the analytical approach adopted by each criterion. Hence, from the same stress-strain values can result different damages depending on the criterion's model. The number of cycles to failure predicted by Dang Van criterion (DV1) is the most conservative while Sines criterion provides slight optimistic life prediction. The calculated fatigue damage value according to Fatemi-Socie criterion shows that the stress-strain field is not damaging enough to cause failure in HCF regime assumed to be corresponding to the range 10^4–10^7 cycles.

A second post-processing calculation has been performed for a blade subject to centrifugal and aerodynamic loads at a steady operating speed of 8000 tr/min. Transient loads due to engine start-up and shutdown was removed from the loading cycles. Results are summarized in Table 6. As reported in Table 6, the stress-strain field is not damaging enough the blade to cause failure in HCF regime. This statement is valid for all the used fatigue criteria and is in compliance with manufacturer recommendations stating that both number of starts and operating number of hours impact the blade fatigue lifetime and decrease the interval for maintenance inspection. Some turbine manufacturers convert each start cycle to an equivalent number of operating hours (EOH) with inspection intervals based on the equivalent hours count (Fig. 17).

Table 5
Estimated blade lifetime – complete loading cycle.

Fatigue criterion	Fatigue damage parameter	Value	Estimated component lifetime
Sines	Maximum equivalent stress (MPa)	312.529	1.42e+6
Crossland	Maximum equivalent stress (MPa)	332.407	1.22e+6
Dang Van-1	Maximum equivalent stress (MPa)	350.744	9.39e+5
Dang Van-2	Maximum equivalent stress (MPa)	332.4	1.22e+6
Fatemi-Socie	Maximum shear strain	8.4e−4	
Fatemi-Socie	maximum normal stress (MPa)	142	
Fatemi-Socie	fatigue damage value D_{FS}	7.5e−4	>1e+7

Table 6
Estimated blade lifetime – loading cycles exempt from start-up and shutdown transient stresses.

Fatigue criterion	Fatigue damage parameter	Value	Estimated component lifetime
Sines	Maximum equivalent stress (MPa)	146.312	>1e+7
Crossland	Maximum equivalent stress (MPa)	146.530	>1e+7
Dang Van-1	Maximum equivalent stress (MPa)	146.540	>1e+7
Dang Van-2	Maximum equivalent stress (MPa)	146.530	>1e+7
Fatemi-Socie	Maximum shear strain	8.94e−6	
Fatemi-Socie	maximum normal stress (MPa)	1.008	
Fatemi-Socie	fatigue damage value D_{FS}	8.93e−6	>1e+7

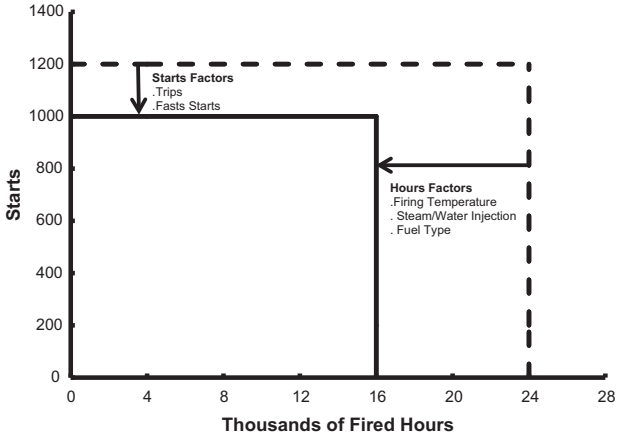

Fig. 17. Factors reducing maintenance interval [31].

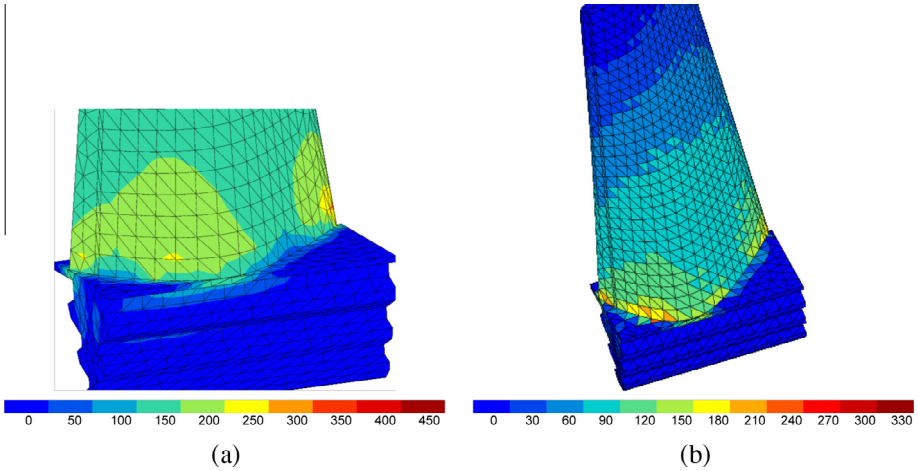

Fig. 18. Maximum von Mises and equivalent fatigue stress values (a) Contour plot of von Mises stress distribution. (b) Contour plot of Crossland equivalent stress values.

For our case, the excessive number of starts [102 starts] in relative short period has definitely reduced the blade's fatigue lifetime to crack initiation and failure as revealed when comparing the estimated blade lifetimes of Tables 5 and 6. It is worth mentioning that although the maximum values of von Mises stress were displayed at the blade trailing edge due to the reduced blade section area (Fig. 18a), the maximum Sines, Crossland and Dang Van equivalent stress values were located at the blade leading edge region close to the blade's root where the crack was initiated (Fig. 18b). Therefore, to accurately predict the location to crack initiation due to fatigue mechanisms, design engineers should not rely only on the area of maximum values of von Mises stress.

5. Conclusion

The present study is focused on the fatigue damage evaluation of a failed gas turbine blade using four multiaxial fatigue models: Sines, Crossland, Dang Van and Fatemi-Socie. Material fatigue parameters required as input to the selected fatigue models were determined through a series of bending and torsion tests on specimens. A numerical post-processing algorithm was developed by the authors for Fatemi-Socie fatigue criterion using the ZeBulon scripting language. Stress and Strain fields have been computed through FEA and post-processing calculations to estimate the blade lifetime during both (i) complete loading cycle including transient loads due to engine start-up and shutdown (ii) and cycle with steady rotating speed. The results achieved in the frame of this study allow to draw the following conclusions:

- The calculated fatigue lifetime predictions are obviously different in terms of number of cycles to failure depending on the damage model due to the fact that the stress-strain fields are processed in different ways respect to the analytical approach adopted by each criterion.
- The fatigue damage criterion which gives the most conservative life predictions is the Dang-Van criterion which is a critical plane criterion taking into account the maximum shear stresses acting on the critical plane and, for this reason, it results to be particularly suitable for ductile metallic materials in HCF regime.
- The post-processing calculations illustrated the effect of transient loads and number of starts in reducing the operating lifetime of the gas turbine blade.
- Contour plots and hot spot regions of von Mises stress distribution are different from fatigue equivalent stress value distributions. It definitely illustrated that the blade's regions of high probability of crack initiation due to fatigue are located at leading edge close to the blade's root and at mid-chord region.

This study completes the initial mechanical and metallography investigations conducted on the failed blade [1] with a fatigue damage assessment and estimated component lifetime to fatigue crack initiation and this through a detailed FEA and post-processing calculations using several multiaxial fatigue criteria. The conducted experiments on Inconel 718 provides as well a useful set of fatigue parameters which could be considered as reliable inputs to other fatigue models.

The next step of this research activity will be the examination of fatigue-crack growth mechanisms and assessment of propagation life.

Acknowledgments

The authors wish to thank BG-Group for supporting and encouraging any advanced technical investigation on failures of equipments in BG assets and CETIM France where the fatigue tests have been conducted.

References

[1] Maktouf W, Saï K. An investigation of premature fatigue failures of gas turbine blade. Eng Fail Anal 2015;47(Part A):89–101.
[2] Dundas R. Engineering and metallographic aspects of gas turbine engine failure investigation: identifying the causes. Flight Saf Found – Aviat Mech Bullet 1994:1–20.
[3] Meher-Homji B, Gabriles G. Gas turbine blade failures – causes avoidance and troubleshooting. Proceedings of the 27th turbomachinery symposium 1995;27:129–80.
[4] Bruun O, Härkegard G. A comparative study of design code criteria for prediction of the fatigue limit under in-phase and out-of-phase tension-torsion cycles. Int J Fatigue 2015;73:1–16.
[5] You B-R, Lee S-B. A critical review on multiaxial fatigue assessments of metals. Int J Fatigue 1996;18:235–44.
[6] Jiang Y, Hertel O, Vormwald M. An experimental evaluation of three critical plane multiaxial fatigue criteria. Int J Fatigue 2007;29:1490–502.
[7] Li B, Reis L, de Freitas M. Comparative study of multiaxial fatigue damage models for ductile structural steels and brittle materials. Int J Fatigue 2009;31:1895–906.
[8] Nicholas T. Critical issues in high cycle fatigue. Int J Fatigue 1999;21 (Supplement 1):S221–31.
[9] Wang Y-Y, Yao W-X. Evaluation and comparison of several multiaxial fatigue criteria. Int J Fatigue 2004;26:17–25.
[10] Morel F, Palin-Luc T, Froustey C. Comparative study and link between mesoscopic and energetic approaches in high cycle multiaxial fatigue. Int J Fatigue 2001;23:317–27.
[11] Han C, Chen X, Kim K. Evaluation of multiaxial fatigue criteria under irregular loading. Int J Fatigue 2002;24:913–22.
[12] Fatemi A, Shamsaei N. Multiaxial fatigue: an overview and some approximation models for life estimation. Int J Fatigue 2011;33:948–58.
[13] Chen H, Shang D-G, Bao M. Selection of multiaxial fatigue damage model based on the dominated loading modes. Int J Fatigue 2011;33:735–9.
[14] Liu Y, Mahadevan S. Multiaxial high-cycle fatigue criterion and life prediction for metals. Int J Fatigue 2005;27:790–800.
[15] H B, Findley WN, Coleman JJ. Theory for combined bending and torsion fatigue with data for 4030 steel. In: International conference on fatigue of metals. New York: The Institution of Mechanical Engineers; 1956.
[16] Fatemi A, Socie DF. A critical plane approach to multiaxial fatigue damage including out of phase loading. Fatigue Fract Eng Mater Struct 1988;11:149–65.
[17] Palin-Luc SLT. A multiaxial fatigue testing machine for variable amplitude loadings of bending and torsion. In: Proceedings of 4th ICBMFF, May 31–June 3, 1994, Paris, vol. 1; 1994. p. 449–59.
[18] Shamsaei N, McKelvey SA. Multiaxial life predictions in absence of any fatigue properties. Int J Fatigue 2014;67:62–72.
[19] Roessle M, Fatemi A. Strain-controlled fatigue properties of steels and some simple approximations. Int J Fatigue 2000;22:495–511.
[20] Kim K, Chen X, Han C, Lee H. Estimation methods for fatigue properties of steels under axial and torsional loading. Int J Fatigue 2002;24(7):783–93.
[21] Muralidharan U, Manson SS. A modified universal slopes equation for estimation of fatigue characteristics of metals. ASME J Eng Mater Technol 1988;110:55–8.
[22] Baumel Jr. A, Seeger T. Materials data for cyclic loading, supplement 1. P.O. Box 211, 1000 AE Amsterdam (The Netherlands): Elsevier Science Publishers; 1990.
[23] Fouchereau R, Celeux G, Pamphile P. Probabilistic modeling of S–N curves. Int J Fatigue 2014;68:217–23.
[24] Klemenc J, Fajdiga M. Estimating S–N curves and their scatter using a differential ant-stigmergy algorithm. Int J Fatigue 2012;43:90–7.
[25] Kohout J, Vechet S. A new function for fatigue curves characterization and its multiple merits. Int J Fatigue 2001;23:175–83.
[26] Sines JLDG, Waisman JL. Metal fatigue. McGraw-Hill; 1959.
[27] Besson J, Leriche R, Foerch R, Cailletaud G. Object-oriented programming applied to the finite element method. Part II. application to material behaviors 1998;7:567–88.
[28] Crossland B. Effect of large hydrostatic pressures on the torsional fatigue strength of an alloy steel. In: Proceedings of international conference on fatigue of metals. London: IMechE; 1956. p. 138–49.
[29] Van KD. Sur la resistance a la fatigue des metaux. Sci Tech l'Armement 1973;47 (3eme fascicule):641–722.
[30] DF S. Critical plane approaches for multiaxial fatigue damage assessment. In: McDowell DL, Ellis R, editors. Advances in multiaxial fatigue. ASTM STP 1191. Philadelphia: Eds. American Society for Testing and Material; 1993. p. 7–36.
[31] Hoeft RKR, Janawitz J. Heavy-duty gas turbine operating and maintenance considerations. In: GER-3620J – GE Energy Services. Atlanta (GA).